

## Probing deformation mechanisms of a FeCoCrNi high-entropy alloy at 293 and 77 K using in situ neutron diffraction

Wang, Yiqiang; Liu, Bin; Yan, Kun; Wang, Minshi; Kabra, Saurabh; Chiu, Yu-Lung; Dye, David; Lee, Peter D.; Liu, Yong; Cai, Biao

DOI:

[10.1016/j.actamat.2018.05.013](https://doi.org/10.1016/j.actamat.2018.05.013)

License:

Creative Commons: Attribution-NonCommercial-NoDerivs (CC BY-NC-ND)

*Document Version*

Peer reviewed version

*Citation for published version (Harvard):*

Wang, Y, Liu, B, Yan, K, Wang, M, Kabra, S, Chiu, Y-L, Dye, D, Lee, PD, Liu, Y & Cai, B 2018, 'Probing deformation mechanisms of a FeCoCrNi high-entropy alloy at 293 and 77 K using *in situ* neutron diffraction', *Acta Materialia*, vol. 154, pp. 79-89. <https://doi.org/10.1016/j.actamat.2018.05.013>

[Link to publication on Research at Birmingham portal](#)

### **Publisher Rights Statement:**

Published in *Acta Materialia* on 10/05/2018

DOI: 10.1016/j.actamat.2018.05.013

### **General rights**

Unless a licence is specified above, all rights (including copyright and moral rights) in this document are retained by the authors and/or the copyright holders. The express permission of the copyright holder must be obtained for any use of this material other than for purposes permitted by law.

- Users may freely distribute the URL that is used to identify this publication.
- Users may download and/or print one copy of the publication from the University of Birmingham research portal for the purpose of private study or non-commercial research.
- User may use extracts from the document in line with the concept of 'fair dealing' under the Copyright, Designs and Patents Act 1988 (?)
- Users may not further distribute the material nor use it for the purposes of commercial gain.

Where a licence is displayed above, please note the terms and conditions of the licence govern your use of this document.

When citing, please reference the published version.

### **Take down policy**

While the University of Birmingham exercises care and attention in making items available there are rare occasions when an item has been uploaded in error or has been deemed to be commercially or otherwise sensitive.

If you believe that this is the case for this document, please contact [UBIRA@lists.bham.ac.uk](mailto:UBIRA@lists.bham.ac.uk) providing details and we will remove access to the work immediately and investigate.

1     **Probing deformation mechanisms of a FeCoCrNi high-entropy alloy at 293 and**  
2                             **77 K using *in situ* neutron diffraction**

3     Yiqiang Wang<sup>a, b</sup>, Bin Liu<sup>c</sup>, Kun Yan<sup>d</sup>, Minshi Wang<sup>e</sup>, Saurabh Kabra<sup>f</sup>, Yu-Lung  
4     Chiu<sup>e</sup>, David Dye<sup>g</sup>, Peter D. Lee<sup>a, f</sup>, Yong Liu<sup>c\*\*</sup>, Biao Cai<sup>e, b\*</sup>,

5     <sup>a</sup> *Culham Centre for Fusion Energy, Culham Science Centre, Abingdon, OX13 3DB,*  
6     *UK*

7     <sup>b</sup> *Research Complex at Harwell, RAL, Harwell, Oxfordshire, OX11 0FA, UK*

8     <sup>c</sup> *The State Key Laboratory of Powder Metallurgy, Central South University, Changsha,*  
9     *410083, P.R. China*

10    <sup>d</sup> *School of Materials, University of Manchester, M13 9PL, UK*

11    <sup>e</sup> *School of Metallurgy and Materials, University of Birmingham, Birmingham*

12    <sup>f</sup> *ISIS Facility, Rutherford Appleton Laboratory, Didcot OX11 0QX, UK*

13    <sup>g</sup> *Department of Materials, Imperial College London, Exhibition Road, London SW7*  
14    *2AZ, United Kingdom*

## Abstract

The deformation responses at 77 and 293 K of a FeCoNiCr high-entropy alloy, produced by a powder metallurgy route, are investigated using *in situ* neutron diffraction and correlative transmission electron microscopy. The strength and ductility of the alloy are significantly improved at cryogenic temperatures. The true ultimate tensile strength and total elongation increased from 980 MPa and 45% at 293 K to 1725 MPa and 55% at 77K, respectively. The evolutions of lattice strain, stacking fault probability, and dislocation density were determined via quantifying the *in situ* neutron diffraction measurements. The results demonstrate that the alloy has a much higher tendency to form stacking faults and mechanical twins as the deformation temperature drops, which is due to the decrease of stacking fault energy (estimated to be 32.5 mJ/m<sup>2</sup> and 13 mJ/m<sup>2</sup> at 293 and 77 K, respectively). The increased volume fraction of nano-twins and twin-twin intersections, formed during cryogenic temperature deformation, has been confirmed by transmission electron microscopy analysis. The enhanced strength and ductility at cryogenic temperatures can be attributed to the increased density of dislocations and nano-twins. The findings provide a fundamental understanding of underlying governing mechanistic mechanisms for the twinning induced plasticity in high entropy alloys, paving the way for the development of new alloys with superb resistance to cryogenic environments.

**Keywords:** high entropy alloy, deformation twinning, neutron diffraction, cryogenic deformation, stacking fault energy

## 1. Introduction

High-entropy alloys (HEAs) were first introduced in 2004 [1, 2], which aimed to maximise the configuration entropy to form a single phase microstructure via combining four or more principle elements in equimolar or near equimolar ratios. The high configuration entropy, sluggish diffusion, cocktail effect and large lattice distortion lead to their promising properties such as high strength, excellent ductility, and superior fracture toughness [3-8].

One type of HEA and its variants, based on five 3d transition elements (Fe, Co, Cr, Mn, Ni), can form a single phase face-centered-cubic (fcc) structure, displaying an excellent combination of high strength, ductility and fracture toughness at both room and cryogenic temperatures. Their mechanical properties improve significantly with decreasing deformation temperatures [3-7]. We termed this group of HEA as tHEA to distinguish them from other high entropy alloys (such as multi-phase HEAs [8]). tHEAs have attracted significant interests for cryogenic applications, such as liquid nitrogen storage and transportation of liquid gas from offshore.

Many microstructural studies [3-7], on strained or failed tensile specimens, have been carried out, confirming the occurrence of nano-twinning during low temperature deformation of tHEAs. Hence twinning induced plasticity is attributed to the tHEAs' superb mechanical performance. Twinning induced plasticity has been at the forefront of research recently as it is one of the micro-mechanistic mechanisms that can overcome the strength-ductility trade-off, which has been demonstrated by fcc metals and alloys with low stacking fault energy (SFE) such as the tHEAs and TWIP steels [9-11].

The deformation mechanisms of fcc metals and alloys are strongly related to the temperature- and composition- dependent stacking fault energy (SFE) [12]. With the drop of SFE, the deformation mechanisms change from dislocation glide alone, to dislocation glide and mechanical twinning, to dislocation glide and martensite transformation [13-15]. This has been demonstrated in many fcc metals and alloys, including austenite steels [16], TRIP and TWIP steels [3,4], and Cu-Al alloys [17]. The SFE of the tHEAs has been measured or calculated to be 10-40 mJ/m<sup>2</sup> at room temperature [18-20]. In this SFE range, deformation twinning is usually activated, which has been confirmed in tHEAs by a few experimental studies [3-7]. Recently, martensite phase transformation have been observed when tHEAs were deformed under hydrostatic high-pressure conditions [21, 22] at both room and high temperatures, demonstrating that the fcc tHEAs can be destabilized into hcp phase at high pressure (e.g. over 14 GPa [21]).

It is known that the SFE will drop as the temperature decreases, hence at cryogenic temperatures, the formation of shear bands, deformation twins and stacking faults can be enhanced [6, 23]. Simulations using first-principles methods [24, 25] confirm the temperature dependent behaviour of SFE and some predict that the SFE of tHEAs can even be negative at cryogenic temperatures [19, 26-28]. To validate the simulated results, the SFE of tHEAs at cryogenic temperatures need to be determined experimentally. Although a few studies have measured room temperature SFE of tHEAs using TEM based methods [18], it is not a straight-forward task to measure low

80 temperature SFE using TEM, as the samples deformed at cryogenic temperatures need  
81 to be warmed up to room temperature for sample preparation, during which the  
82 dislocation and fault structure may have changed. Thereby the development of new  
83 methods to measure low temperature SFE is critically needed, which will provide  
84 much-needed validation for the simulations[19, 26] and pave the way for designing new  
85 tHEAs.

86 To study deformation mechanisms of tHEAs, quantitative *in situ* mapping of  
87 microstructure evolution of tHEAs at room temperature has previously been carried out,  
88 using TEM [26, 29, 30], SEM [31], synchrotron X-ray diffraction [32] and neutron  
89 diffraction [33, 34]. The *in situ* TEM directly observed the motion of Shockley partials,  
90 the formation of stacking faults and 3D network of nano-twins [29, 30]. *In situ* neutron  
91 and X-ray diffraction, on the other hand, can quantify the grain-level behaviour during  
92 deformation, which includes the measurement of stacking fault probability [33], single-  
93 crystal elastic constants [34], phase transformation [32], and SFE [33]. Those *in situ*  
94 works significantly improved our understanding of the microstructural and mechanistic  
95 origin of tHEAs' superb mechanical properties. Carrying out *in situ* studies at cryogenic  
96 temperatures can provide similar benefits, not only unravelling the underlying  
97 mechanisms determining the dramatic increase of strength and ductility at cryogenic  
98 temperatures of the alloys, but also determining critical material parameters such as  
99 SFE.

In the current study, we conducted uniaxial tensile deformation on a FeCoCrNi high-entropy alloy at 293 and 77 K. With the help of *in situ* neutron diffraction, we monitored and quantified the microstructural responses during tensile deformation, including the evolution of lattice strain, stack fault probability and dislocation density versus imposed strain at both temperatures. The different responses between 293 and 77 K were compared. We also calculated the stacking fault energy of the alloy at both 293 and 77 K. TEM observations were carried out on the deformed samples, providing correlative analysis. The work provides in-depth micro-mechanistic understanding involving the complex interaction of stacking faults, twins and dislocations for the studied tHEAs at cryogenic temperatures, which could pave the way for designing advanced metallic materials resistant to cryogenic environments.

## **2. Experimental details**

The FeCoCrNi high entropy alloy was fabricated by powder metallurgical processes, which are detailed in Refs. [33, 35], namely, hot extrusion of gas-atomized FeCoCrNi powders. The alloy has a single fcc structure and the average grain size of the as-extruded specimen was approximately 35  $\mu\text{m}$ . The mechanical properties and microstructure of the alloy at room temperature can be found in Ref. [35].

*In situ* time-of-flight neutron diffraction measurements during tensile deformation were performed on the ENGIN-X neutron diffractometer, Rutherford Appleton Laboratory (RAL), ISIS, UK [36, 37]. A stress rig with a load capability of 100 kN was used for the experiments. An in-house built cold chamber, integrated with the stress rig, was used which provides a controlled cryogenic temperature environment (10-293 K) [38].

A schematic of the setup is shown in Fig. 1a. A low temperature extensometer was used to measure the displacement of the part of gauge length (10 mm). The rig was mounted on the diffractometer horizontally. The loading axis was oriented horizontally, parallel to the extruded direction and orientated  $45^\circ$  relatives to the incident beam. The two detectors (axial and radial) allow collection of the diffraction patterns at fixed horizontal scattering angles of  $\pm 90^\circ$ , with diffraction vectors parallel and perpendicular to the loading direction, respectively.

Dog bone-shaped uniaxial tensile specimens with a gauge length of 34.5 mm and diameter of 8 mm were prepared from the as-extruded material. A  $4 \times 4 \times 4 \text{ mm}^3$  neutron measurement gauge volume was used. Diffraction patterns were acquired for 20 min intervals between tensile loading steps, iterating until the sample failed. During the cooling down process for the cryogenic temperature deformation test, a stress level of 5 MPa was maintained via stress-control. During loading up, a stress-control was used before the yielding point, which was followed by strain-control. The diffraction spectra was analysed by Open G software which provides the information of d-spacing, peak intensity and full width at half maximum (FWHM).

In order to calculate the stacking fault energy and dislocation density from the measured diffraction spectra, single peak fitting with a pseudo-voigt convolution was developed in Matlab. The measured diffraction patterns, after being deconvoluted with the instrument function, can be described by the convolution of a Gaussian and a Lorentz function.



$$I(x) = I(0) \left[ \mu \exp \left[ -\pi \frac{(x - x_0)^2}{\beta_G^2} \right] + (1 - \mu) \frac{1}{\frac{\beta_C^2}{\pi^2} + (x - x_0)^2} \right] \quad (1)$$

143 where  $x_0$  is the peak centre, and  $\beta_G$  and  $\beta_C$  are constant parameters of the Guassian and  
 144 Lorentz respectively.  $\mu$  and  $(1-\mu)$  denote the fraction of Guassian and Lorentz used. The  
 145 size strain and microstrain contribution are then related to the parameters of the  
 146 Guassian and Lorentz function by

$$D_{eff} = \frac{1}{\beta_c} \quad (2)$$

147 And

$$\langle \xi^2 \rangle_{hkl}^{1/2} = \left( \frac{2}{\pi} \right)^{1/2} \beta_G d_{hkl} / 2 \quad (3)$$

148 respectively.  $D_{eff}$  is the effective dimension of coherently diffraction blocks (e.g. grains)  
 149 and  $\xi$  is the microstrain and its root-mean-square could be interpreted to be proportional  
 150 to the square root of dislocation density ( $\rho^{1/2}$ ) as follows:

$$\rho = \frac{k \langle \xi^2 \rangle}{F b^2} \quad (4)$$

151 where  $b$  represents the magnitude of Burgers vector.  $F$  and  $k$  are two constants, and  $F$   
 152 =1 and  $k = 1.61\text{nm}$  were chosen according to [39] for fcc crystal with a Burgers vector  
 153 along  $\langle 110 \rangle$ .

154 Transmission electron microscopy (TEM) study was conducted on a JEOL-2100 TEM  
 155 operated at 200 kV to examine the microstructure of the specimens after the *in situ*  
 156 neutron diffraction experiments. The TEM samples were extracted from regions close

to and away from the fracture surfaces which represent samples with different strain levels. On the sample deformed at 77 K, TEM foils were extracted from the regions with cross-section diameters equal to 6.8 mm and 6.24 mm which correspond to reduction in the cross section area ( $\psi$ ) during the tensile test of 27.8% and 39.2%, respectively. For sample deformed at 293 K, TEM foils were extracted from the regions with the cross-section diameters equal to 7.15 and 6.47 mm which correspond to the reduction in cross section area ( $\psi$ ) during the tensile test of 20.1% and 34.6%, respectively. The foils extracted were ground down to  $\sim 80 \mu\text{m}$ , then disks of 3 mm diameter were punched out and twin-jet electro-polished in a solution containing 100 mL  $\text{HClO}_4$  and 900 mL  $\text{CH}_3\text{COOH}$  at approximately  $-10^\circ\text{C}$ .

### **3. Results and discussion**

#### **3.1 Mechanical properties**

Fig. 1b shows the true stress-true strain curves of the polycrystalline FeCoCrNi alloy tensile deformed to fracture at 77 and 293 K. The yield strength (YS) and ultimate tensile strength (UTS) increase from approximately 260MPa and 980MPa at 273 K to 480MPa and 1725 MPa at 77 K. The total elongation also increases from about 45% to 55% (corresponding to engineering strain of 55% and 72% respectively) as the test temperature is decreased from 293 to 77 K. This enhancement of strength and ductility of the tHEA alloys at cryogenic temperatures is also compared to a few selected previous studies, as summarized in Tab. 1. It can be shown that the yield strength and UTS often increased 1.5-2 times while the maximum elongation often increased 10-15% when the deformation temperature was dropped from 293 to 77 K. The mechanical

properties of FeCoCrNiMo<sub>0.23</sub> alloy at both temperatures are also provided in Table 1 for comparison. It shows that micro-alloying the tHEA with Mo enhances the mechanical properties.

The strain hardening rate (SHR), which represents by the derivative of the true stress with respect to the true strain, is shown in Fig. 1c as a function of true stress. The area below the line  $d\sigma/d\varepsilon = \sigma$  reveals the region in which necking is predicted to occur according to Considre's criterion. The SHRs of the alloy at 77 and 293 K show a similar trend, whereas two distinguished stages can be found in both curves – rapid drop of the strain hardening rate at small stress level, then the decrease slows down at higher stress. The transition points between the two stages are marked in Fig. 1b. The transition point for room temperature tensile test is at 410 MPa (5.6 %) true stress (strain) level, whereas at 77 K, it is 682 MPa (6.3 %) true stress (strain). The SHR at 77 K is higher than at room temperature, which is consistent with other studies [5, 6, 23].

In summary, the FeCoCrNi alloy has significantly improved strength, ductility and strain hardening capability at 77 K than at room temperature. The underlying mechanisms will be discussed with the help of *in situ* neutron diffraction and correlative electron microscopies in the following sections.

### 3.2 The evolution of lattice strain

As shown in Fig. 2, the tHEA is a fcc single phase structure at both 293 and 77 K before deformation. The lattice parameters at 293 and 77 K are 0.3604 and 0.3563 nm, respectively, calculated by the average of five diffraction peaks. Cooling the sample to cryogenic temperature results in the drop of lattice parameter. During the course of

deformation at both 293 and 77 K, the tHEA stays as a fcc structure (no additional peaks belongs to bcc and hcp structure appears), which means that martensite transformation do not occur in this alloy.

The changes in lattice strains can be calculated using

$$\varepsilon_{hkl} = \frac{d_{hkl} - d_{hkl}^0}{d_{hkl}^0} \quad (4)$$

where  $\varepsilon_{hkl}$  is the lattice strain in the  $\{hkl\}$  grain family,  $d_{hkl}$  is the current sample lattice spacing and  $d_{hkl}^0$  is the stress-free lattice spacing. The stress-free lattice spacing was taking from the measurement point at 5 MPa at the temperatures.

Elastic lattice strains along the axial and radial directions in grain families having  $\{111\}$ ,  $\{200\}$ ,  $\{220\}$ ,  $\{311\}$  and  $\{222\}$  crystallographic planes during tensile deformation at 77 and 293K, are shown in Fig. 2a and 2b, respectively. The uncertainties in the measured internal strains were approximately 30 microstrain [40].

Fig. 2a shows that the lattice strains increased with applied stress linearly from 0 to 450 MPa, and then nonlinearly when the applied stress was greater than 450MPa during tensile loading at 77 K. This is due to the fact that the load transfers from softer grain families (e.g. 220) to harder grain families (e.g. 200) [33]. The trend of lattice strain evolution at 293 K is similar to that at 77 K, except the nonlinear transition happened earlier than that at 77 K (above  $\sim 250$ MPa). Overall, at 77 K, the lattice strain values of all grain families in the axial direction are larger than at 293 K under similar deformation level.

We determined grain orientation dependent diffraction elastic constants ( $E_{hkl}$ ) and Poisson's ratios ( $V_{hkl}$ ) through fit linear responses to the purely elastic parts of each curve in Fig. 2.  $E_{\text{Rietveld}}$  and  $V_{\text{Rietveld}}$  have also determined through preform the Rietveld fitting of 8 peaks. All these values are listed in Tab. 2. The  $E_{hkl}$  values are very similar for both temperatures. The  $E_{\text{Rietveld}}$ ,  $V_{\text{Rietveld}}$  and  $V_{hkl}$ , are slightly lower at cryogenic temperatures than room temperature. Daymond et al. [41] show that the value of  $E_{\text{Rietveld}}$  is very similar to the macroscopic Young's modulus. The current temperature dependent values of  $E_{\text{Rietveld}}$  are compared with the temperature dependent Young's moduli of CoCrFeMnNi in Ref. [42] with excellent agreement.

### 3.3 Stacking fault probability

Before we start analysing the stacking fault probability (SFP), we shall note the relationship between twins and stacking faults. Upon deformation, passage of Shockley partial dislocation with Burger vector  $1/6\langle 112 \rangle$  on neighbouring two (111) planes creates an intrinsic stacking fault, and continuous passage of the partial dislocations on successive (111) planes creates multi-layer faults forming twin nucleuses; in the end larger twins can be formed by passage of more partials on neighbouring (111) planes [43]. For alloys with stacking fault between  $18 < \text{SFE} < 45 \text{ mJ/m}^2$ , twinning is more favourable to occur with external straining. At SFE values  $< 18 \text{ mJ/m}^2$ , martensite formation occurs when the molar Gibbs energy of martensitic is negative. This martensitic transformation takes place either by fcc-hcp, or, for even lower SFE, martensite formation by fcc-hcp-bcc becomes the favoured transformation mechanism that affects the further deformation of the material [13]. The fcc to hcp transformation

can occur by shifting every two neighboring fcc (111) planes in the  $[11-2]$  direction by a distance of  $a/\sqrt{6}$  (where  $a$  is the lattice parameter), which is realised by the partial dislocation movements in the (111) planes [14]. When SFE exceeds  $45 \text{ mJ/m}^2$ , plasticity and strain hardening are controlled solely by the glide of dislocations [15].

Many studies [33, 44-46] have shown that stacking faults, if they occur in fcc crystals, can change the Bragg scattering positions compared with a fault-free lattice. The peak position shifts for successive orders of reflections such as {111} and {222} might be different arising from the structure factor for stacking faults. This can be used to estimate the stacking fault density in the sample.

We plot the lattice strain evolutions of {111} and {222} at axial and radial directions for 77 and 293 K tensile tests in Fig. 4a and 4b, respectively. The separation of {111} and {222} lattice strain in the axial direction after certain amount of strain is obvious for both temperatures, which indicates the formation of stacking faults and possibly twins in grains whose  $\{hkl\}$  plane-normals oriented “parallel” to the loading axis. Interestingly, at room temperature, the {111} and {222} lattice strain curves in the radial detector bank, almost overlap for the sample deformed. However, at 77K, the two lattice strain show distinct difference. The radial detector registers a portion of the grains whose  $\{hkl\} \perp$  plane-normals are “perpendicular” to the loading axis. The results suggest that those grains registered are unfavourable for twinning at room temperature but form stacking faults and twins at 77 K. In addition, it shows that twinning and stacking fault formation are strongly orientation-dependent (e.g. grains

264 with  $\{hkl\}$  plane-normal oriented “parallel” to the loading axis are easier to form  
 265 stacking faults and twins). At cryogenic temperature, twin nucleation and growth can  
 266 be triggered in grains whose orientation is unfavourable for twinning at room  
 267 temperatures.

268 Both  $(hkl)$  dependent macro-strain ( $\varepsilon_{hkl}^{strain}$ ) and stacking faults ( $\varepsilon_{hkl}^{sf}$ ) can contribute to  
 269 the change of lattice strain ( $\varepsilon_{hkl}^{exp}$ ) measured by the peak shift in the experiment. The  
 270 measured lattice strain ( $\varepsilon_{hkl}^{exp}$ ),  $(hkl)$  dependent macro-strain ( $\varepsilon_{hkl}^{strain}$ ) and stacking  
 271 faults ( $\varepsilon_{hkl}^{sf}$ ) follow a relationship:

$$\varepsilon_{hkl}^{exp} = \varepsilon_{hkl}^{strain} - \varepsilon_{hkl}^{sf} = \varepsilon_{hkl}^{strain} - \frac{\sqrt{3}}{4\pi} \frac{\sum_b \pm(h+k+l)}{(u+b)(h^2+k^2+l^2)} SFP \quad (7)$$

272 where  $u$  and  $b$  are the numbers of non-broadened and broadened component due to  
 273 stacking faults; SFP represents stacking fault probability. With the help of Eq. (7), we  
 274 are able to calculate the stacking fault probability, which directly indicates the density  
 275 of stacking faults.

276 The evolution of the stacking fault probability during loading up at 77 and 293 K  
 277 obtained from Eq. 7 are shown in Fig. 4a and 4b. At 77 K, the SFP increases from 0 to  
 278  $3 \times 10^{-3}$  after true strain reaches approximately 4.8%. After this, the SFP increases  
 279 almost linearly with the increase of true strain, especially after the true strain is larger  
 280 than 10%. The SFP increases to  $25.6 \times 10^{-3}$  at the strain level of 47% (close to failure).  
 281 At 293 K, the SFP fluctuates below 0 when the true strain is smaller than 10%. After

10% true strain, the SFP becomes positive and increases with true strain steadily up to  $5.4 \times 10^{-3}$  at the strain level of 48.6%, which is about five times smaller than that at 77 K. The evolutions of SFP with applied true strains for both temperatures can be fitted with a linear function in the true strain range from 3% to 55% (Fig. 4a and 4b). The slope at 77 K is 0.72, which is about three times larger than that at 293K (0.24).

The fact that at 77 K, compared to room temperature, the sample shows much higher SFP at similar strain level and the SFP curve is much steeper, suggests that at low temperatures, the FeCoCrNi alloy can form more stacking faults in the sample and the nucleation and growth of twins might be much quicker than at room temperature.

We then plot the SFP as a function of true stress of the FeCoNiCr and FeCoNiCrMo<sub>0.23</sub> at both 77 and 293 K, as shown in Fig. 4c. For both alloys, the SFP values of the two deformation temperatures almost overlap at the same stress level when the true stress is over roughly 450 MPa. This implies that the density of stacking faults of tHEAs is mainly a function of stress levels, regardless of deformation temperature. FeCoNiCrMo<sub>0.23</sub> alloy shows similar behaviour. At the same stress, the alloy with Mo addition has a slightly higher SFP.

### 3.4 Stacking fault energy

The stacking fault energy (SFE) represents the easiness of dissociating a perfect dislocation into two partial dislocations and the tendency for the formation of SFs. It can be calculated by Reed and Schramm's equation [47]. Note that the SFE we



302 measured here by neutron diffraction is the so-called intrinsic stacking fault energy  
 303 ( $\gamma_{ISF}$ ).

$$\gamma_{ISF} = \frac{6.6a_0}{\pi\sqrt{3}} \left( \frac{2c_{44}}{c_{11} - c_{12}} \right)^{-0.37} \frac{\langle \xi^2 \rangle_{111}}{SFP} \left( \frac{c_{44} + c_{11} - c_{12}}{3} \right) \quad (8)$$

304 where,  $\gamma_{ISF}$  is the intrinsic stacking fault energy,  $a_0$  is the lattice parameter.  
 305  $\langle \xi^2 \rangle_{111}$  is the mean square microstrain, which is obtained by an integral breadth  
 306 method with a pseudo-voigt convolution [48]. The single crystal elastic constants  
 307 (SCEC) ( $C_{11}$ =271.0 GPa,  $C_{12}$  = 175.0 GPa, and  $C_{44}$ =189.3 GPa) are adopted from *ab*  
 308 *initio* atomistic simulation on an fcc FeCoNiCr alloy at 0 K [49]. The SCEC varies only  
 309 slightly between 77 K and room temperature according to the simulation work [25].  
 310 The stacking fault probability is measured at around engineering strain level of 48% for  
 311 both temperatures. The SFE of the FeCoCrNi high-entropy alloy is then estimated by  
 312 Eq. 8 to be 13 mJ/m<sup>2</sup> at 77 K and 32.5 mJ/m<sup>2</sup> at 293 K (Tab. 3). Expression (8),  
 313 however, is still approximate and we cannot determine reliable error values. There are  
 314 likely errors related to the calculation of the mean square micro-strain. Also, the  
 315 variation of SCEC between different temperatures and the measurement of SCEC by  
 316 atomistic simulation is not taken into account and may add additional uncertainty in the  
 317 estimated SFE due to many assumptions included in the model [49]. However,  
 318 measurements of SCEC is very limited and we would expect that accurately measuring  
 319 SCEC, both by experiments and simulation as a function of temperature, will provide  
 320 a more robust determination of SFE using eq. 8. We also estimated the SFE of a

FeCoNiCrMo<sub>0.23</sub> to be 19 mJ/m<sup>2</sup> at room temperature [33] and 10 mJ/m<sup>2</sup> at 77 K (Table 3), which is lower than that of the FeCoNiCr alloy, suggesting that micro-alloying of Mo can reduce the stacking fault energy of the tHEAs.

The estimated SFE at room temperature (32.5 mJ/m<sup>2</sup>) agrees with the experimental measurement on FeCoCrNi tHEA by the combined use of XRD and DFT simulation (e.g. 17.4, 34.3 and 31.7 mJ/m<sup>2</sup> depending on alloy composition used [50]) and TEM (27±4 mJ/m<sup>2</sup> [19]). Currently no experimental measurement of tHEAs' SFE at cryogenic temperature is reported. Only a few simulations were performed on FeCoNiCr alloy. Zhao *et al.* performed ab initio calculation on a series of fcc tHEAs. Their results show that the SFE of FeCoNiCr stays negative at 0 K. Depending on which models they used, the predicted SFE values vary around -20 mJ/m<sup>2</sup> [19] ). Zhang *et al.* [26] reported that SFE at 0 K of fcc FeCoNiCr falls from -82 to -180 mJ/m<sup>2</sup>. Beyramali Kivvy and Asle Zaeem's simulation gives a SFE value of 31.6±0.9 mJ/m<sup>2</sup> [19] although the temperature at which the simulation was carried out is not reported. Our estimation of SFE at 77 K may provide a validation for SFE simulations if one can carry out the *ab initio* calculations at different temperatures such as the one performed by Huang *et al.* on a FeCrCoNiMn alloy [25]. Their work obtains an SFE of 8 mJ/m<sup>2</sup> at 77 K on FeCrCoNiMn alloy, which is slightly lower than our measurement on the FeCrCoNi alloy, indicating that variations in Mn contents can cause a change to SFE values.

The SFE is a critical parameter in the deformation properties of fcc metals and alloys. The SFE influences phenomena such as the capacity of a dislocation to cross slip, the

formation of partial dislocation and twin boundaries [51]. Low SFE can lead to the domination of a highly planar slip on a well-defined (111) plane, suppressing dislocation cross-slip, hence augmenting the yield strength [51]. Additionally, Norihiko *et al.* [52] suggest that the increase of yield stress at cryogenic temperature of tHEAs is due to the thermal component of solid-solution hardening. The increase of yield stress at cryogenic temperature is due to both the thermal component of solid-solution hardening and the suppression of dislocation cross-slip. The very low SFE of the tHEA used in this study strongly supports the conclusion from section 3.3 that the alloy is prone to form twins when strained. Additionally, the drop of SFE at cryogenic temperatures suggests that more deformation twins are able to nucleate and grow when deformed at lower temperatures.

### 3.5 Critical stress for twinning ( $\sigma_{tw}$ )

Experimental determination of  $\sigma_{tw}$  is challenging. It has been obtained via identifying the transition point in the work hardening curve [53], or through careful TEM observation on interrupted strained specimens [23, 35]. The critical stress for twinning was measured by a few studies using TEM previously, which demonstrates that the critical stress for twinning was independent of temperature and estimated to be  $\sim 720 \pm 30$  MPa for FeCrNiCoMn alloy [35] and  $790 \pm 100$  MPa for CrCoNi alloy [23]. The criteria used in those studies for determining the critical twinning stress level is that nano-twins start to be identified by TEM.

As we noted before, the stacking fault probability we measured is directly related to the density of stacking faults. Hence the SFP curve might allow us to estimate critical points of stacking fault and twinning formation. The SFP stays negative at very low strains, and when it reaches over 0, it increases continuously as we increase deformation. The first critical point we identify is when the stacking fault probability becomes positive (just above 0). We use the linearly fitted equations (Fig. 4) to determine the stress level at SFP=0, which are  $450\pm30$  MPa/9.6% strain at 77K and  $500\pm15$  MPa/0.717% strain at 293 K. This point might mark the nucleation stage of stacking fault within the sample as when stacking faults start to form, the peak positions of the (111) and (222) planes begin to shift apart, reflecting the contribution from the stacking fault. However, due to the large scattering of the SFP at lower strain levels, those values should be used with cautions.

The second critical point we consider is when  $SFP = 0.003$  (the purple line in Fig. 4a and 4b), at which sufficient and sizable stacking faults should have formed, lead to the nucleation of twin faults. The corresponding true stress values are  $730\pm30$  MPa/21.2% strain at 293 K and  $635\pm30$  MPa/4.885% strain at 77 K (Table 3). The measurement is consistent with previous studies using TEM [23, 35], suggesting that the SFP curve could be a reliable way to measure the critical stress for twinning.

With regards to the twinning stress prediction, two approaches have been developed. The classic approach, based on theories such as Venables' pole mechanism [54] and the Manajan-Chin stacking fault process [55], predicts that the critical resolved shear

stress for twinning ( $\tau_{twin}$ ) is proportional to intrinsic stacking fault energy ( $\gamma_{isf}$ ) [53]  
 ( $\tau_{twin} \times b_p \sim \gamma_{isf}$ ). Based on this, various equations have been formulated, and we  
 choose a few as shown in Table 4, together with the twinning stress values predicted  
 based on the equations. The predicted twinning stress values seem to be temperature  
 dependent. A significant discrepancy among different equations can also be observed.  
 The huge variations of twinning stress among different models demonstrate that a  
 systematic validation of the models with experiments is critically needed. Narita and  
 Takamura's and Venable's models predict relatively low  $\sigma_{tw}$ . It is even lower than the  
 yield strength at 77 K. Byun's model, on the other hand, gives relatively high values.  
 According to Byun's model, a twinning stress of 1353 MPa is needed to prompt  
 deformation twin at room temperature, which is above the UTS of the alloy. If this is  
 the case, deformation twinning is very unlikely to form during room temperature  
 deformation, unless some grains experience significant stress concentration. This is in  
 contradiction with our TEM observation (TEM confirms the formation of nano-twins  
 within the tensile strained sample, section 3.8). It has been suggested that Byun's model  
 overestimates the twinning stress in TWIP steels [53], which seems to be the case  
 according to our result. The twinning stresses predicted by Steinmetz *et al.* model (661  
 MPa at 77K, 799 MPa at 293 K) seems to agree reasonably well with the twinning stress  
 values we determined from the SFP curves (635 MPa at 77K, 730 MPa at 293 K).  
 Steinmetz *et al.* model, based on Mahajan-Chin three-layer twinning mechanism, has  
 also been shown to accurately predict the twinning stress in TWIP steels [53].

It has been suggested that intrinsic SFE alone is not sufficient to predict deformation twinning mechanisms [53]. The generalized planar fault energy concept, recently developed, has proposed that the stacking fault formation and twinning process are controlled by the energy barriers, rather than just the intrinsic stacking fault energy. The energy barriers include the intrinsic stacking fault energy, the unstable stacking fault energy, the extrinsic stacking fault energy and the unstable twin fault energy [53]. The twinning stress is then directly correlated to the unstable twinning fault energy, together with the intrinsic stacking fault energy. However, to determine the unstable twinning fault energy by experiments is not possible, and it usually requires using first principle calculation. Hence, to accurately determine the critical twinning stress, *ab initio* calculation needs to be performed, which should be validated against the experimental values via the combined use of interrupted TEM investigation [23, 35] and *in situ* diffraction methods as demonstrated here.

### 3.6 Evolution of dislocation density

The higher strain hardening rate at 77 K could result from the high dislocation density in fcc matrix as well as the interaction between dislocations and nano-twins. Here, the dislocation density during tensile deformation at 77 and 293 K are measured using Eq. 3, which are shown in Fig. 5a as a function of true strain. It indicates that the dislocation density increases as the strains/stress increases. At the cryogenic temperature, a much higher density of dislocations is accumulated after plastic deformation. A linear

equation ( $\rho = \rho_0 + K\varepsilon$ ) can be used to describe the dislocation density and true strain relationship:

$$\rho = 1.4 \times 10^{15} + 7.6 \times 10^{13} \varepsilon \quad (10)$$

$$\text{and } \rho = 1.5 \times 10^{15} + 3.5 \times 10^{13} \varepsilon \quad (11)$$

at 77 and 293 K, respectively.

The increases in the tensile stress,  $\Delta\sigma$ , due to forest dislocation interactions can be described by:

$$\Delta\sigma = \alpha M G b \rho^{1/2} \quad (12)$$

where  $\alpha$  is a constant,  $M$  is the Taylor factor (3.06),  $G$  is the shear modulus (85 GPa at 77 K; 80 GPa at 293K [42, 56]),  $b$  is the magnitude of the Burgers vector (0.252 nm at 77 K and 0.253 nm at 293 K) and  $\rho$  is the dislocation density. Fig. 5b shows the normalized increment of stresses  $(\sigma - \sigma_y)/MG$  (where  $\sigma$  is the current stress) at both 77 and 293 K, which can be fitted with a linear function. Only data beyond the yielding is included. The slope of the linear function at 77 K is 0.53 which agrees with that found in CrMnFeCoNi [6]. The slope of the linear function at 293 K is 0.95, which almost doubles the value at 77 K. However, we note that the physical meaning of  $\alpha$  is not very clear hence it is hard to interpret, and Eq. 12 ignores the contribution from the other sources including dislocation-mechanical twin boundary interaction.

Gini *et al.* [57] proposed an equation that incorporates Eq. 12 and the plasticity model of Nes and Marthinsen [58]:

$$\Delta\sigma = \alpha M G b \rho^{1/2} + \frac{M \beta G b}{\Lambda} \quad (13)$$

where  $\Lambda$  is the dislocation mean free path, and  $\beta$  is a constant. The formation of mechanical twins reduces the dislocation mean free path. Thereby, according to Eq.13, it is the dynamic increase of boundaries, due to the formation of mechanical twinning, together with the continuously increase of dislocation density that leads to the enhanced strain hardening behaviour of the tHEA during plastic deformation.

### 3.7 Peak intensity

Fig. 6 also shows the normalized peak intensity evolution of several lattice reflections parallel and perpendicular to the load axis versus true stress. A few points can be drawn regarding the changes of peak intensity and the differences at 77 and 293K:

- (i) The peak intensity of the axial (220) decreased significantly when the applied load was larger than the macroscopic yielding, as shown in Fig. 6. The (220) peak at axial direction almost vanished when the applied stress was above 1500 MPa at 77 k and 800 MPa at 293 K. The fact that the (220) peak disappears when the sample is strained close to failure in both samples is very interesting and has been observed before in a FeCoNiCrMo<sub>0.23</sub> alloy as well. In contrast, the peak intensity of 220 at radial direction increased by a factor of 1.1 to 2 during the whole deformation.



(ii) The peak intensity of (200) at both axial and radial directions increased significantly at 77 K, but hardly changed at 293K.

(iii) For (111) and (222) grains families, the peak intensity increased in axial direction by a factor of 3 at 77 K but decreased in radial direction. The final peak intensity of (222) and (111) changed by a factor of ~5.5 at 293 K.

Significant difference in peak intensity evolution at 77 and 293 K was observed, signifying the different behaviour in terms of the re-orientation of grains during the tensile deformation, which could be due to slip/rotation of grains [59] and/or formation of mechanical twins [60]. However, it is not easy to distinguish the contribution from grain rotation and mechanical twins.

### 3.8 Microstructure characterisation

The microstructures of the deformed specimens after the *in situ* neutron studies were analysed by transmission electron microscopy (TEM) in order to gain a better understanding of the controlling deformation mechanisms. TEM bright field (BF) images and selected area diffraction patterns (SADP) of the samples deformed at 77 and 293 K are shown in Figs. 7 and 8, respectively, showing that nano-sized lamellas have formed to accommodate strain when the sample was deformed at both temperatures. The lamellas are twin structure as confirmed by the diffraction patterns in Fig. 7d and 8d. TEM samples for Fig. 7a and 7b are taken from the failed *in situ* samples at different reductions in cross-section area ( $\psi$ ). The twin-twin intersections can also be readily observed in Fig. 7a and 7b, which can form a complex 3-dimensional network inhibiting dislocation propagation. Fig. 7a and 7b also show that at 77 K more

twins are formed at higher strain level. Comparing Fig. 7 with Fig.8, we conclude that less twins and twin-twin intersections are formed at room temperature, consistent with our measurement from *in situ* neutron diffraction. We do not observe martensite phase at both temperature through TEM, again, consistent with our observation by neutron diffraction (Fig. 2). A further drop of deformation temperature might lead to the formation of martensite as SFE will become ever lower.

The dramatic increase of nano-twins and twin-twin intersections at lower temperatures plays a key role for the higher strain hardening ability the alloy achieved at 77 K than 293 K as shown in Fig. 1b. The combination of enhanced dislocation hardening (higher dislocation density during cryogenic deformation) and mechanical twinning (higher twin volume fraction during cryogenic deformation) provide a larger work hardening rate during tensile deformation at 77 K than at 293 K.

#### 4. Conclusions

In our work, we fabricated a FeCoNiCr high entropy alloy with a single phase fcc structure using a powder metallurgy route. We used *in situ* neutron diffraction to map the evolution of deformation microstructure at both 77 and 293 K, correlatively characterized by TEM. Several conclusions can be drawn based on the experimental results:

1. The alloy has a good combination of high ultimate tensile strength (UTS ~1725 MPa) and ductility (elongation~55%) at 77 K, which is much higher than the room temperature properties (UTS ~ 980 MPa, and elongation ~45%). Higher

501 strain hardening rate is also obtained at cryogenic temperature than at room  
502 temperature.

503 2. Via *in situ* neutron diffraction measurement, we are able to determine the  
504 stacking fault probability (SFP) as a function of stress level at both 77 and 293  
505 K. The SFP increases much quicker and reaches a much higher value at similar  
506 strain levels at cryogenic temperature than room temperature.

507 3. Using diffraction line profile analysis, stacking fault energy is estimated to be  
508  $\sim 13 \text{ mJ/m}^2$  at 77 K and  $\sim 32.5 \text{ mJ/m}^2$  at 293 K. As the SFE drops at cryogenic  
509 temperature, more twin faults form as the alloy is deformed at cryogenic  
510 temperatures. Nano-twins at both 77 and 293 K of the alloy have been observed  
511 by TEM, and at 77 K, many more twins and twin-twin intersections are formed  
512 than at room temperature.

513 4. We used the stacking fault probability curve to determine the critical stress for  
514 twinning. The critical stress for twinning is set to stress levels when the SFP is  
515 0.003. The corresponding true stress values are  $730 \pm 30 \text{ MPa}$  at 293 K and  
516  $635 \pm 30 \text{ MPa}$  at 77 K, which agree with previous measurements on  
517 CrCoNi and CrMnFeCoNi alloys as well as Steinmetz *et al.* model.

518 5. Dislocation density is calculated for both temperatures from neutron diffraction  
519 spectra. Higher dislocation density is found during low temperature plastic  
520 deformation than at room temperature.

6. The combination of dislocation hardening and mechanical twinning provides large work hardening rate and high strength during tensile deformation for the high entropy alloy. The superior mechanical properties at the cryogenic temperature is attributed to the enhanced dynamic Hall-Petch hardening and dislocation hardening as at lower temperatures, increased amount of nano-twins and dislocation are formed.

## **Acknowledgements**

The authors thank ISIS (the Rutherford Appleton Laboratory, UK) for providing the beamtime (RB1610297) and staff at EnginX beamline for support. Y.Q.W. and P.D.L. acknowledge the support provided by the Research Complex at Harwell, funded in part by EPSRC ((EP/K007734/1 and EP/L018705/1).. B.C. acknowledges the support from Diamond Birmingham Collaboration. Y.L. and B.L. acknowledge the National Natural Science Foundation of China (51671217), and the Projects of Innovation-driven Plan in Central South University of China (2015CX004).

## Tables

Table 1. Comparison of yield strength (YS), ultimate tensile strength (UTS), and total elongation obtained at 77K and 293K from the present study to selected prior studies.

Materials	Temp. (K)	YS (MPa)	UTS (MPa)	Elongation (%)
FeCoCrNi	77	480	1725	55
	293	260	980	45
FeCoCrNiMo <sub>0.23</sub>	77	602	1863	51
	293	360	1238	48
CrCoNi [23]	77	560	1625	44
	293	360	750	30
CrMnFeCoNi [6]	77	460	1060	60
	293	265	600	45

541  
542  
543  
544

Table 2. Uniaxial materials properties of FeCoCrNi HEA at 77 and 293 K

Temp.	a	E <sub>111</sub>	E <sub>200</sub>	E <sub>220</sub>	E <sub>311</sub>	E <sub>Rietveld</sub>	V <sub>111</sub>	V <sub>200</sub>	V <sub>220</sub>	V <sub>311</sub>	V <sub>Rietveld</sub>
(K)	(nm)	(GPa)	(GPa)	(GPa)	(GPa)	(GPa)					
77	0.3563	146.3	97.0	191.6	214.0	229	0.138	0.232	0.168	0.234	0.20
293	0.3604	136.6	98.0	175.0	237.2	190	0.198	0.349	0.348	0.321	0.27

545  
546

Table 3. Stacking fault energy of FeCoCrNi tHEA at 77 and 293 K

	FeCoCrNi	FeCoCrNi	FeCoCrNiMo <sub>0.23</sub>	FeCoCrNiMo <sub>0.23</sub>
Temperature	77 K	293 K	77 K	293 K
SFE (mJ/m <sup>2</sup> )	13	32.5	10	19
Twinning Stress	635 ± 30	730 ± 30	-	-

Table 4. Critical stress for twinning of FeCoCrNi tHEA at 77 and 293 K

Sources	Equations	Temp.	$\tau_{tw}$ (MPa)	$\sigma_{tw}$ (MPa)
Narita and Takamura [55]	$\tau_{tw} = \frac{\gamma_{isf}}{2b_p}$	77 K	45	135
		293 K	110	337
Venable [54, 61]	$\tau_{tw} = \frac{b\gamma_{isf}}{b_p(nb - b_p)}$	77 K	37-63	113-193
		293 K	91-155	278-474
Byun [62]	$\tau_{tw} = \frac{2\gamma_{isf}}{b_p}$	77 K	178	545
		293 K	442	1353
Steinmetz <i>et al.</i> [63]	$\tau_{tw} = \frac{\gamma_{isf}}{3b_p} + \frac{3Gb_p}{L_0}$	77K	216	661
		293 K	261	799

\*  $n$  is the stress-concentration factor ( $n=1$  represents no stress concentration while  $n \geq 3$  means static tension, here  $n = 2-3$ ) [20];

\*  $L_0$  is the width of a twin embryo (approximately 200 nm);

\*  $\sigma_{tw} = M\tau_{tw}$ , where  $M$  is the Taylor factor.

## List of figures

Fig. 1. (a) Schematic of the in situ neutron diffraction set-up; (b) True stress-strain curves of uniaxial tensile tests at 77 K and 293 K and (c) the corresponding working hardening rate versus true stress.

Fig. 2. Diffraction patterns collected at the axial detector as a function of stress at (a) 293 K; and (b) 77 K.

Fig. 3. The evolution of elastic lattice strains along the axial and radial directions in grain families having {111}, {200}, {220}, {311} and {222} crystallographic planes during tensile loading at (a) 77 K and (b) 293 K;

Fig. 4. The (111) first order and (222) second order reflections together with the stacking fault probability as a function of true strain at (a) 77 K and (b) 293 K.

Fig. 5. The evolution of dislocation density versus (a) true strain, and (b) normalised work hardening  $(\sigma - \sigma_y)/MG$  versus  $b\rho^{1/2}$ .

Fig. 6. The evolution of normalized peak intensity along the axial and radial directions in grain families having {111}, {200}, {220}, {311} and {222} crystallographic planes during tensile loading at (a) 77 K and (b) 293 K.

Fig. 7. TEM bright field micrographs of samples with (a) 27.8 % and (b) 39.2% strain at 77 K, which show nano-twins. (c) Higher magnification BF images with an inserted SAD pattern obtained from the matrix and (f) the composite SAD pattern obtained from the blue circled region in Fig. 7c which has contribution from both the matrix and the nano-twin.

Fig. 8. TEM bright field micrographs of samples with (a) 20.1% and (b) 34.6% strain at 293k, which show nano-twins. (c) Higher magnification BF images with an inserted SAD pattern obtained from the matrix and (f) the composite SAD pattern obtained from the blue circled region in Fig. 8c which has contribution from both the matrix and the nano-twin.



595 **Reference**

- 596 [1] B. Cantor, I. Chang, P. Knight, A. Vincent, Microstructural development in  
597 equiatomic multicomponent alloys, *Materials Science and Engineering: A* 375 (2004)  
598 213-218.
- 599 [2] J.W. Yeh, S.K. Chen, S.J. Lin, J.Y. Gan, T.S. Chin, T.T. Shun, C.H. Tsau, S.Y.  
600 Chang, Nanostructured high-entropy alloys with multiple principal elements: novel  
601 alloy design concepts and outcomes, *Advanced Engineering Materials* 6(5) (2004) 299-  
602 303.
- 603 [3] B. Gludovatz, A. Hohenwarter, D. Catoor, E.H. Chang, E.P. George, R.O. Ritchie,  
604 A fracture-resistant high-entropy alloy for cryogenic applications, *Science* 345(6201)  
605 (2014) 1153-1158.
- 606 [4] F. Otto, A. Dlouhý, C. Somsen, H. Bei, G. Eggeler, E.P. George, The influences of  
607 temperature and microstructure on the tensile properties of a CoCrFeMnNi high-  
608 entropy alloy, *Acta Materialia* 61(15) (2013) 5743-5755.
- 609 [5] J. Moon, S.I. Hong, J.W. Bae, M.J. Jang, D. Yim, H.S. Kim, On the strain rate-  
610 dependent deformation mechanism of CoCrFeMnNi high-entropy alloy at liquid  
611 nitrogen temperature, *Materials Research Letters* (2017) 1-6.
- 612 [6] G. Laplanche, A. Kostka, O. Horst, G. Eggeler, E. George, Microstructure evolution  
613 and critical stress for twinning in the CrMnFeCoNi high-entropy alloy, *Acta Materialia*  
614 118 (2016) 152-163.
- 615 [7] A. Gali, E.P. George, Tensile properties of high-and medium-entropy alloys,  
616 *Intermetallics* 39 (2013) 74-78.
- 617 [8] Z. Li, K.G. Pradeep, Y. Deng, D. Raabe, C.C. Tasan, Metastable high-entropy dual-  
618 phase alloys overcome the strength–ductility trade-off, *Nature* 534(7606) (2016) 227.
- 619 [9] D.T. Pierce, J.A. Jiménez, J. Bentley, D. Raabe, J.E. Wittig, The influence of  
620 stacking fault energy on the microstructural and strain-hardening evolution of Fe–Mn–  
621 Al–Si steels during tensile deformation, *Acta Materialia* 100 (2015) 178-190.
- 622 [10] K. Yan, D.G. Carr, M.D. Callaghan, K.-D. Liss, H. Li, Deformation mechanisms  
623 of twinning-induced plasticity steels: In situ synchrotron characterization and  
624 modeling, *Scripta Materialia* 62(5) (2010) 246-249.
- 625 [11] K. Rahman, V. Vorontsov, D. Dye, The effect of grain size on the twin initiation  
626 stress in a TWIP steel, *Acta Materialia* 89 (2015) 247-257.
- 627 [12] M. Jo, Y.M. Koo, B.-J. Lee, B. Johansson, L. Vitos, S.K. Kwon, Theory for  
628 plasticity of face-centered cubic metals, *Proceedings of the National Academy of*  
629 *Sciences* 111(18) (2014) 6560-6565.
- 630 [13] S. Curtze, V.-T. Kuokkala, Dependence of tensile deformation behavior of TWIP  
631 steels on stacking fault energy, temperature and strain rate, *Acta materialia* 58(15)  
632 (2010) 5129-5141.

- [14] K. Tao, J.J. Wall, H. Li, D.W. Brown, S.C. Vogel, H. Choo, In situ neutron diffraction study of grain-orientation-dependent phase transformation in 304L stainless steel at a cryogenic temperature, *Journal of applied physics* 100(12) (2006) 123515.
- [15] O. Grässel, L. Krüger, G. Frommeyer, L. Meyer, High strength Fe–Mn–(Al, Si) TRIP/TWIP steels development—properties—application, *International Journal of plasticity* 16(10-11) (2000) 1391-1409.
- [16] H. Barman, A. Hamada, T. Sahu, B. Mahato, J. Talonen, S. Shee, P. Sahu, D. Porter, L. Karjalainen, A Stacking Fault Energy Perspective into the Uniaxial Tensile Deformation Behavior and Microstructure of a Cr–Mn Austenitic Steel, *Metallurgical and Materials Transactions A* 45(4) (2014) 1937-1952.
- [17] Y. Tian, L. Zhao, S. Chen, A. Shibata, Z. Zhang, N. Tsuji, Significant contribution of stacking faults to the strain hardening behavior of Cu-15% Al alloy with different grain sizes, *Scientific reports* 5 (2015) 16707.
- [18] X. Xu, P. Liu, Z. Tang, A. Hirata, S. Song, T. Nieh, P. Liaw, C. Liu, M. Chen, Transmission electron microscopy characterization of dislocation structure in a face-centered cubic high-entropy alloy Al<sub>0.1</sub>CoCrFeNi, *Acta Materialia* 144 (2018) 107-115.
- [19] S. Liu, Y. Wu, H. Wang, J. He, J. Liu, C. Chen, X. Liu, H. Wang, Z. Lu, Stacking fault energy of face-centered-cubic high entropy alloys, *Intermetallics* (2017).
- [20] H. Diao, R. Feng, K. Dahmen, P. Liaw, Fundamental deformation behavior in high-entropy alloys: An overview, *Current Opinion in Solid State and Materials Science* (2017).
- [21] C.L. Tracy, S. Park, D.R. Rittman, S.J. Zinkle, H. Bei, M. Lang, R.C. Ewing, W.L. Mao, High pressure synthesis of a hexagonal close-packed phase of the high-entropy alloy CrMnFeCoNi, *Nature communications* 8 (2017) 15634.
- [22] F. Zhang, S. Zhao, K. Jin, H. Bei, D. Popov, C. Park, J.C. Neumeier, W.J. Weber, Y. Zhang, Pressure-induced fcc to hcp phase transition in Ni-based high entropy solid solution alloys, *Applied Physics Letters* 110(1) (2017) 011902.
- [23] G. Laplanche, A. Kostka, C. Reinhart, J. Hunfeld, G. Eggeler, E. George, Reasons for the superior mechanical properties of medium-entropy CrCoNi compared to high-entropy CrMnFeCoNi, *Acta Materialia* 128 (2017) 292-303.
- [24] P. Sahu, S. Shee, A. Hamada, L. Rovatti, T. Sahu, B. Mahato, S.G. Chowdhury, D. Porter, L. Karjalainen, Low strain rate deformation behavior of a Cr–Mn austenitic steel at – 80° C, *Acta Materialia* 60(20) (2012) 6907-6919.
- [25] S. Huang, W. Li, S. Lu, F. Tian, J. Shen, E. Holmström, L. Vitos, Temperature dependent stacking fault energy of FeCrCoNiMn high entropy alloy, *Scripta Materialia* 108 (2015) 44-47.
- [26] Y. Zhang, Y. Zhuang, A. Hu, J. Kai, C. Liu, The origin of negative stacking fault energies and nano-twin formation in face-centered cubic high entropy alloys, *Scripta Materialia* 130 (2017) 96-99.
- [27] Z. Zhang, H. Sheng, Z. Wang, B. Gludovatz, Z. Zhang, E.P. George, Q. Yu, S.X. Mao, R.O. Ritchie, Dislocation mechanisms and 3D twin architectures generate

exceptional strength-ductility-toughness combination in CrCoNi medium-entropy alloy, *Nature communications* 8 (2017) 14390.

[28] S. Zhao, G.M. Stocks, Y. Zhang, Stacking fault energies of face-centered cubic concentrated solid solution alloys, *Acta Materialia* 134 (2017) 334-345.

[29] Z. Zhang, M. Mao, J. Wang, B. Gludovatz, Z. Zhang, S.X. Mao, E.P. George, Q. Yu, R.O. Ritchie, Nanoscale origins of the damage tolerance of the high-entropy alloy CrMnFeCoNi, *Nature communications* 6 (2015) 10143.

[30] J. Liu, C. Chen, Y. Xu, S. Wu, G. Wang, H. Wang, Y. Fang, L. Meng, Deformation twinning behaviors of the low stacking fault energy high-entropy alloy: An in-situ TEM study, *Scripta Materialia* 137 (2017) 9-12.

[31] M. Wang, Z. Li, D. Raabe, In-situ SEM observation of phase transformation and twinning mechanisms in an interstitial high-entropy alloy, *Acta Materialia* 147 (2018) 236-246.

[32] L. Ma, L. Wang, Z. Nie, F. Wang, Y. Xue, J. Zhou, T. Cao, Y. Wang, Y. Ren, Reversible deformation-induced martensitic transformation in Al 0.6 CoCrFeNi high-entropy alloy investigated by in situ synchrotron-based high-energy X-ray diffraction, *Acta Materialia* 128 (2017) 12-21.

[33] B. Cai, B. Liu, S. Kabra, Y. Wang, K. Yan, P.D. Lee, Y. Liu, Deformation mechanisms of Mo alloyed FeCoCrNi high entropy alloy: In situ neutron diffraction, *Acta Materialia* 127 (2017) 471-480.

[34] Y. Wu, W. Liu, X. Wang, D. Ma, A.D. Stoica, T. Nieh, Z. He, Z. Lu, In-situ neutron diffraction study of deformation behavior of a multi-component high-entropy alloy, *Applied Physics Letters* 104(5) (2014) 051910.

[35] B. Liu, J. Wang, Y. Liu, Q. Fang, Y. Wu, S. Chen, C. Liu, Microstructure and mechanical properties of equimolar FeCoCrNi high entropy alloy prepared via powder extrusion, *Intermetallics* 75 (2016) 25-30.

[36] J. Santisteban, M. Daymond, J. James, L. Edwards, ENGIN-X: a third-generation neutron strain scanner, *Journal of Applied Crystallography* 39(6) (2006) 812-825.

[37] S.Y. Zhang, A. Evans, E. Eren, B. Chen, M. Pavier, Y. Wang, S. Pierret, R. Moat, B. Mori, ENGIN-X—instrument for materials science and engineering research, *Neutron News* 24(3) (2013) 22-26.

[38] O. Kirichek, J. Timms, J. Kelleher, R. Down, C. Offer, S. Kabra, S. Zhang, Sample environment for neutron scattering measurements of internal stresses in engineering materials in the temperature range of 6 K to 300 K, *Review of Scientific Instruments* 88(2) (2017) 025103.

[39] G. Williamson, R. Smallman, III. Dislocation densities in some annealed and cold-worked metals from measurements on the X-ray debye-scherrer spectrum, *Philosophical Magazine* 1(1) (1956) 34-46.

[40] Y. Wang, S. Hossain, S. Kabra, S. Zhang, D. Smith, C. Truman, Effect of boundary conditions on the evolution of lattice strains in a polycrystalline austenitic stainless steel, *Journal of Materials Science* 52(13) (2017) 7929-7936.

[41] M. Daymond, M. Bourke, R. Von Dreele, B. Clausen, T. Lorentzen, Use of Rietveld refinement for elastic macrostrain determination and for evaluation of plastic

strain history from diffraction spectra, *Journal of Applied Physics* 82(4) (1997) 1554-1562.

[42] G. Laplanche, P. Gadaud, O. Horst, F. Otto, G. Eggeler, E. George, Temperature dependencies of the elastic moduli and thermal expansion coefficient of an equiatomic, single-phase CoCrFeMnNi high-entropy alloy, *Journal of Alloys and Compounds* 623 (2015) 348-353.

[43] S. Kibey, J. Liu, D. Johnson, H. Sehitoglu, Predicting twinning stress in fcc metals: Linking twin-energy pathways to twin nucleation, *Acta materialia* 55(20) (2007) 6843-6851.

[44] J. Jeong, W. Woo, K. Oh, S. Kwon, Y. Koo, In situ neutron diffraction study of the microstructure and tensile deformation behavior in Al-added high manganese austenitic steels, *Acta Materialia* 60(5) (2012) 2290-2299.

[45] J. Jeong, Y. Koo, I. Jeong, S. Kim, S. Kwon, Micro-structural study of high-Mn TWIP steels using diffraction profile analysis, *Materials Science and Engineering: A* 530 (2011) 128-134.

[46] J.t. Cohen, C. Wagner, Determination of twin fault probabilities from the diffraction patterns of fcc metals and alloys, *Journal of Applied Physics* 33(6) (1962) 2073-2077.

[47] R. Reed, R. Schramm, Relationship between stacking-fault energy and x-ray measurements of stacking-fault probability and microstrain, *Journal of Applied Physics* 45(11) (1974) 4705-4711.

[48] S. Harjo, Y. Tomota, P. Lukáš, D. Neov, M. Vrana, P. Mikula, M. Ono, In situ neutron diffraction study of  $\alpha$ - $\gamma$  Fe-Cr-Ni alloys under tensile deformation, *Acta materialia* 49(13) (2001) 2471-2479.

[49] F. Tian, L.K. Varga, N. Chen, L. Delczeg, L. Vitos, Ab initio investigation of high-entropy alloys of 3 d elements, *Physical Review B* 87(7) (2013) 075144.

[50] A. Zaddach, C. Niu, C. Koch, D. Irving, Mechanical properties and stacking fault energies of NiFeCrCoMn high-entropy alloy, *Jom* 65(12) (2013) 1780-1789.

[51] J.P. Hirth, J. Lothe, *Theory of dislocations*, (1982).

[52] N.L. Okamoto, S. Fujimoto, Y. Kambara, M. Kawamura, Z.M. Chen, H. Matsunoshita, K. Tanaka, H. Inui, E.P. George, Size effect, critical resolved shear stress, stacking fault energy, and solid solution strengthening in the CrMnFeCoNi high-entropy alloy, *Scientific reports* 6 (2016) 35863.

[53] B.C. De Cooman, Y. Estrin, S.K. Kim, Twinning-induced plasticity (TWIP) steels, *Acta Materialia* 142 (2018) 283-362.

[54] J. Venables, Deformation twinning in face-centred cubic metals, *Philosophical magazine* 6(63) (1961) 379-396.

[55] N. Naeita, J. Takamura, Deformation twinning in silver-and copper-alloy crystals, *Philosophical Magazine* 29(5) (1974) 1001-1028.

[56] A. Haglund, M. Koehler, D. Catoor, E. George, V. Keppens, Polycrystalline elastic moduli of a high-entropy alloy at cryogenic temperatures, *Intermetallics* 58 (2015) 62-64.

- [57] G. Dini, R. Ueji, A. Najafizadeh, S. Monir-Vaghefi, Flow stress analysis of TWIP steel via the XRD measurement of dislocation density, *Materials Science and Engineering: A* 527(10) (2010) 2759-2763.
- [58] E. Nes, K. Marthinsen, Modeling the evolution in microstructure and properties during plastic deformation of fcc-metals and alloys—an approach towards a unified model, *Materials Science and Engineering: A* 322(1) (2002) 176-193.
- [59] W. Woo, E.-W. Huang, J.-W. Yeh, H. Choo, C. Lee, S.-Y. Tu, In-situ neutron diffraction studies on high-temperature deformation behavior in a CoCrFeMnNi high entropy alloy, *Intermetallics* 62 (2015) 1-6.
- [60] D. Brown, M. Bourke, M. Stout, P. Dunn, R. Field, D. Thoma, Uniaxial tensile deformation of uranium 6 wt pct niobium: a neutron diffraction study of deformation twinning, *Metallurgical and Materials Transactions A* 32(9) (2001) 2219-2228.
- [61] J.W. Christian, S. Mahajan, Deformation twinning, *Progress in materials science* 39(1-2) (1995) 1-157.
- [62] Y.-F. Shen, Y. Wang, X.-P. Liu, X. Sun, R.L. Peng, S.-Y. Zhang, L. Zuo, P.K. Liaw, Deformation mechanisms of a 20Mn TWIP steel investigated by in situ neutron diffraction and TEM, *Acta Materialia* 61(16) (2013) 6093-6106.
- [63] D.R. Steinmetz, T. Jäpel, B. Wietbrock, P. Eisenlohr, I. Gutierrez-Urrutia, A. Saeed-Akbari, T. Hickel, F. Roters, D. Raabe, Revealing the strain-hardening behavior of twinning-induced plasticity steels: Theory, simulations, experiments, *Acta Materialia* 61(2) (2013) 494-510.

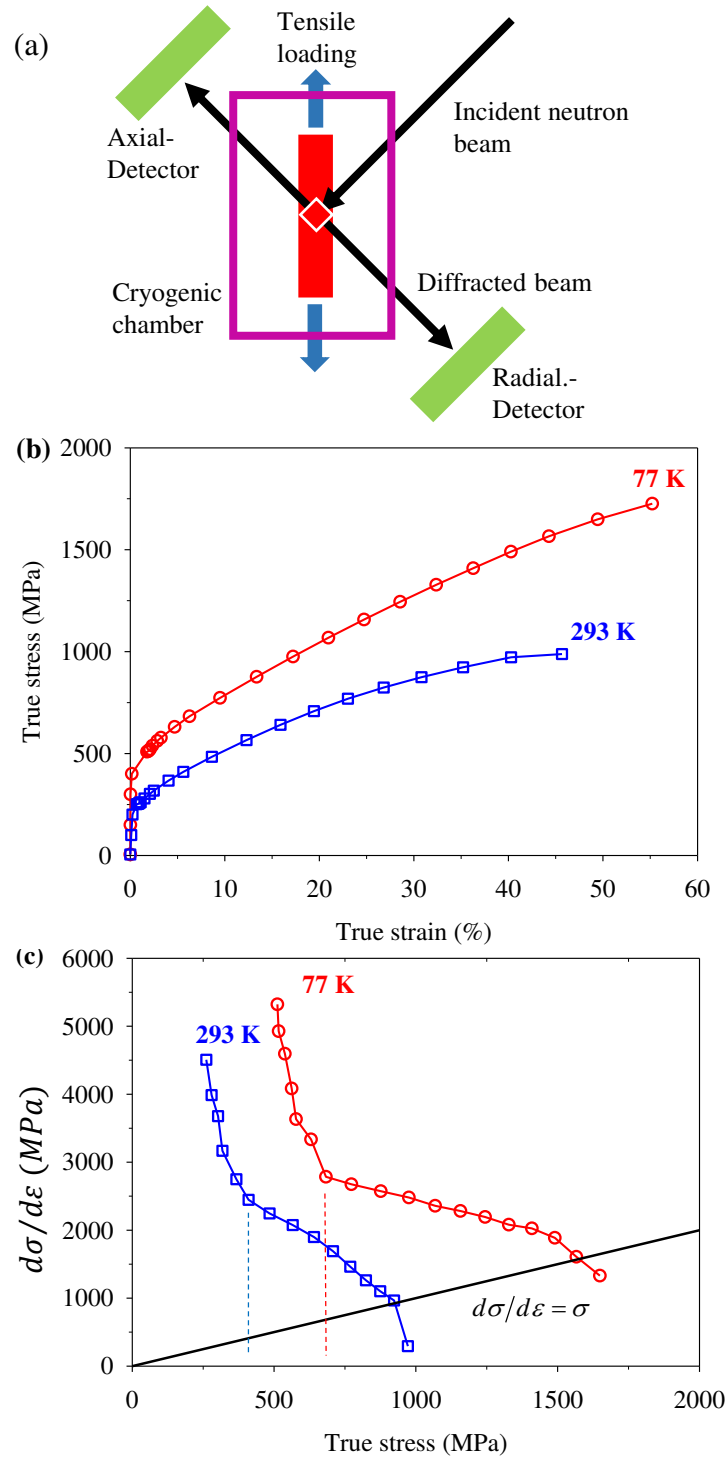


Fig. 1. (a) Schematic of the *in situ* neutron diffraction set-up; (b) True stress-strain curves of uniaxial tensile tests at 77 K and 293 K and (c) the corresponding work hardening rate versus true stress.

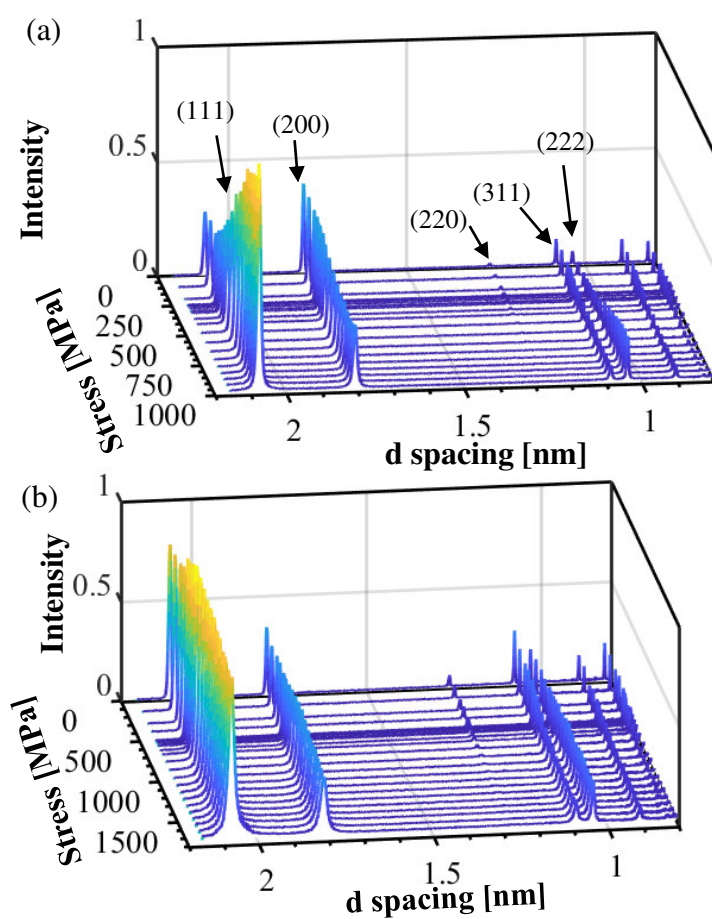


Fig. 2. Diffraction patterns collected at the axial detector as a function of stress at (a) 293 K; and (b) 77 K.

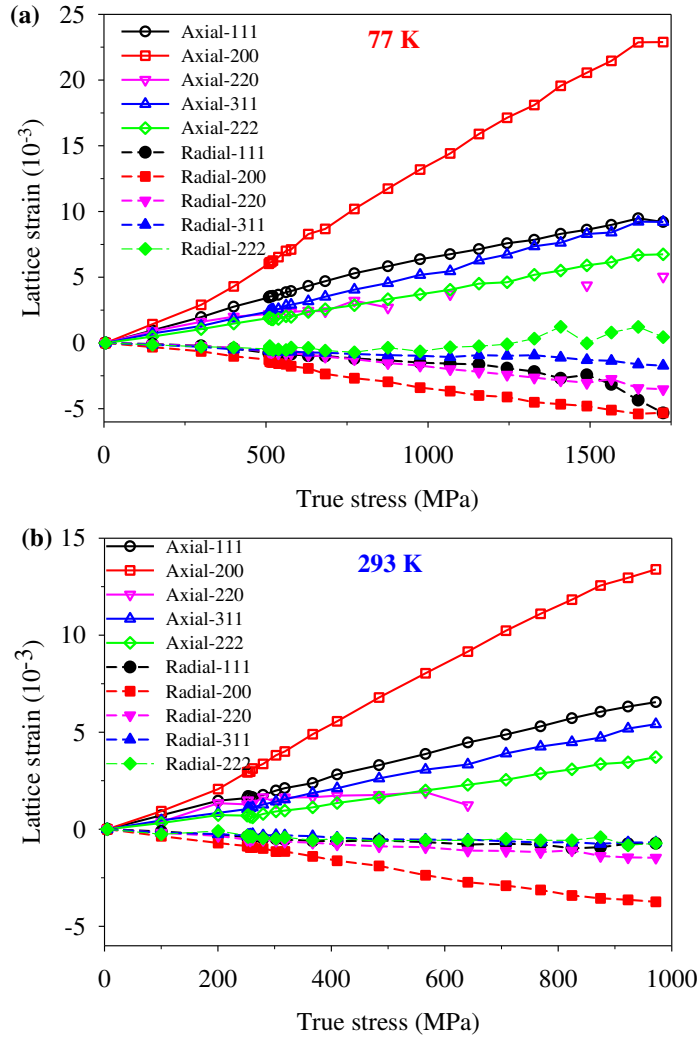


Fig. 3. The evolution of elastic lattice strains along the axial and radial directions in grain families having  $\{111\}$ ,  $\{200\}$ ,  $\{220\}$ ,  $\{311\}$  and  $\{222\}$  crystallographic planes during tensile loading at (a) 77 K and (b) 293 K;



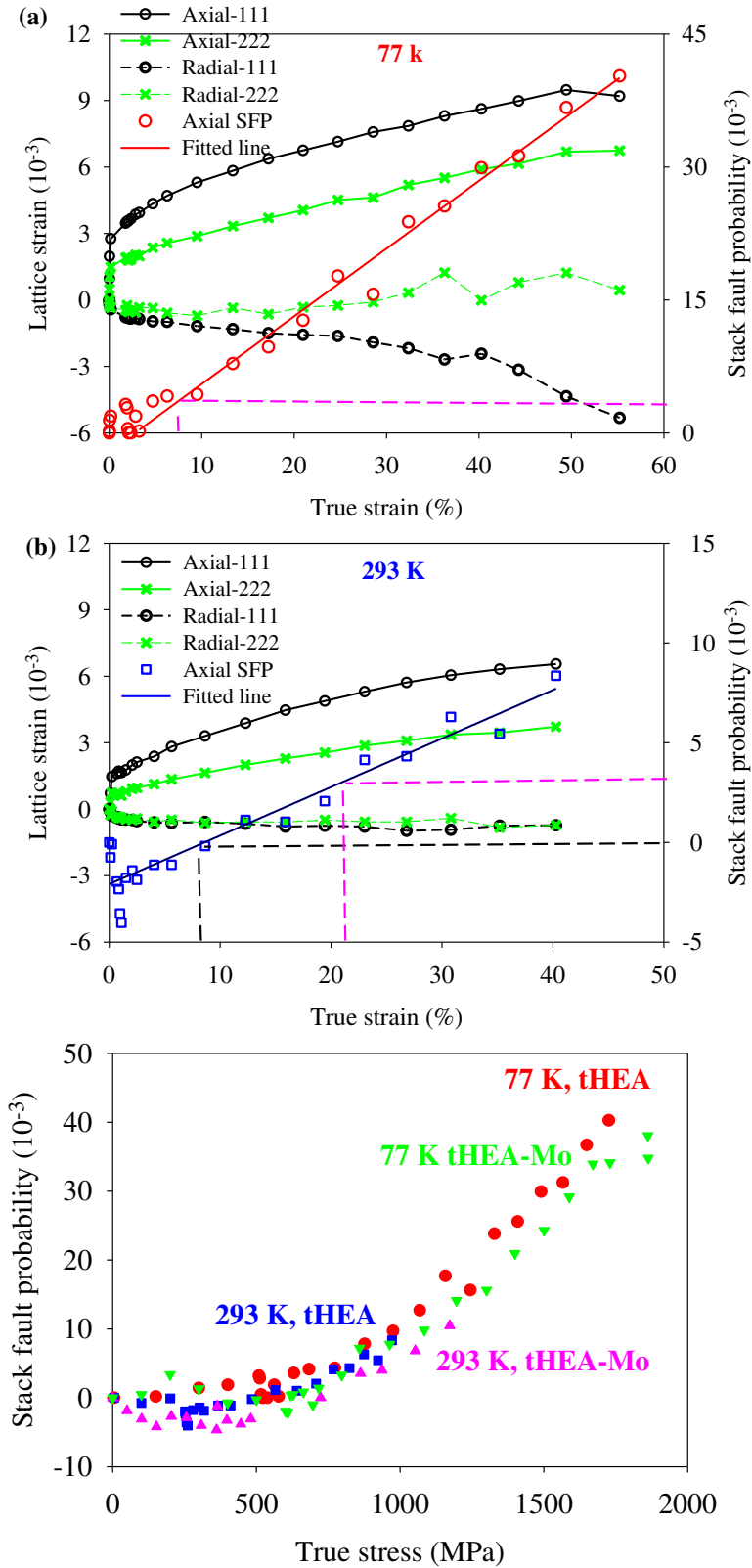


Fig. 4. The (111) first order and (222) second order reflections together with the stacking fault probability as a function of true strain at (a) 77 K and (b) 293 K; (c) stacking fault probability as a function of true stress (tHEA: FeCoCrNi; tHEA-Mo: FeCoCrNiMo<sub>0.23</sub>).

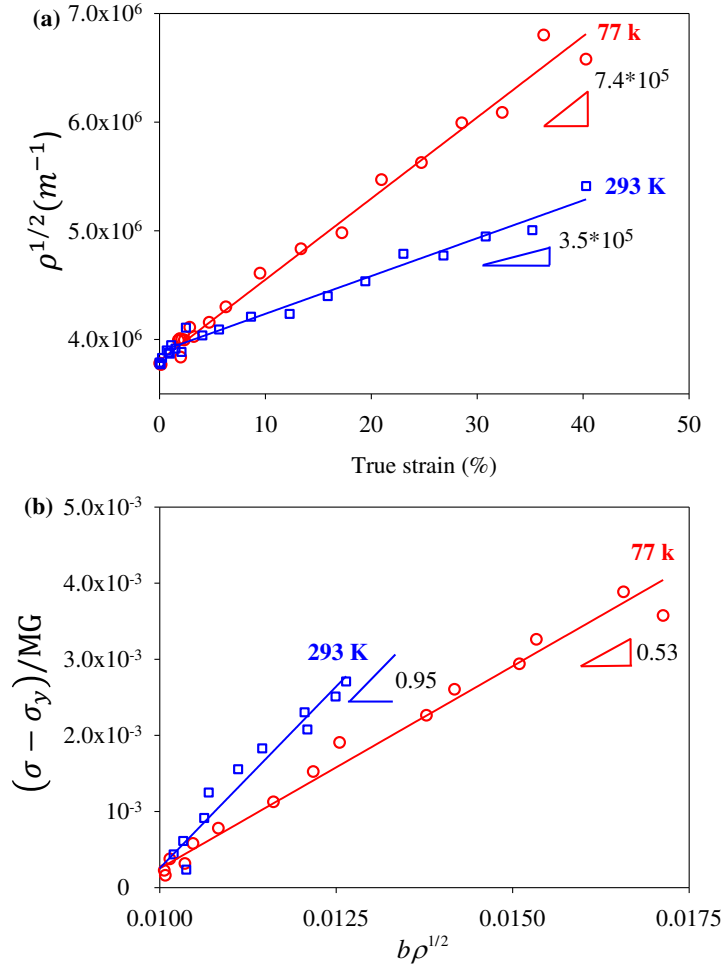


Fig. 5. The evolution of dislocation density versus (a) true strain, and (b) normalised work hardening  $(\sigma - \sigma_y)/MG$  versus  $b\rho^{1/2}$ .

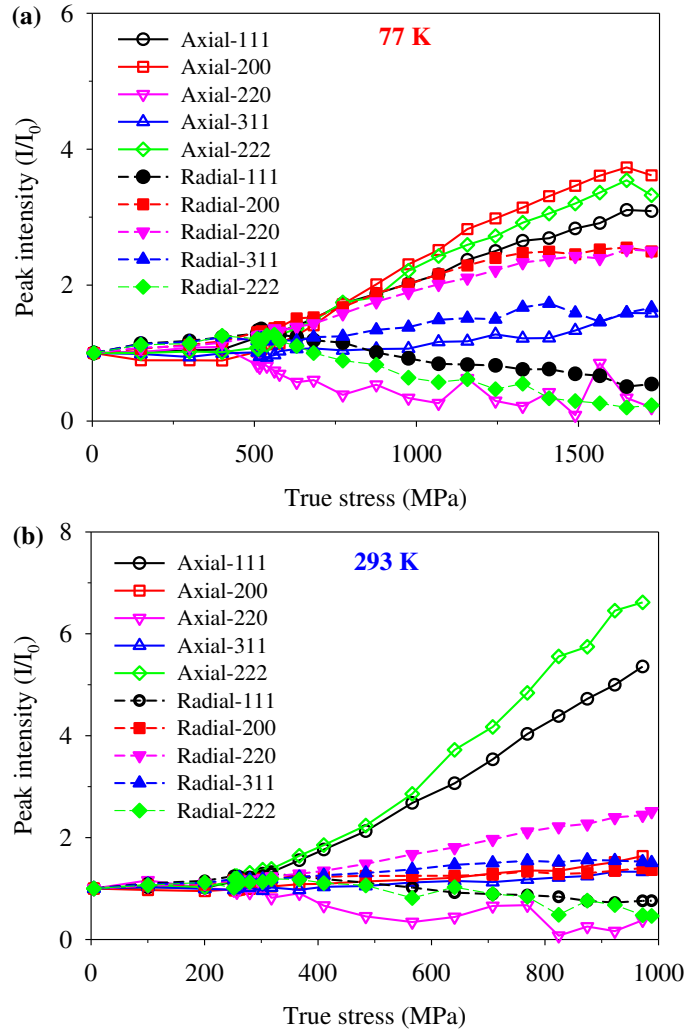


Fig. 6. The evolution of normalized peak intensity along the axial and radial directions in grain families having {111}, {200}, {220}, {311} and {222} crystallographic planes during tensile loading at (a) 77 K, and (b) 293 K.

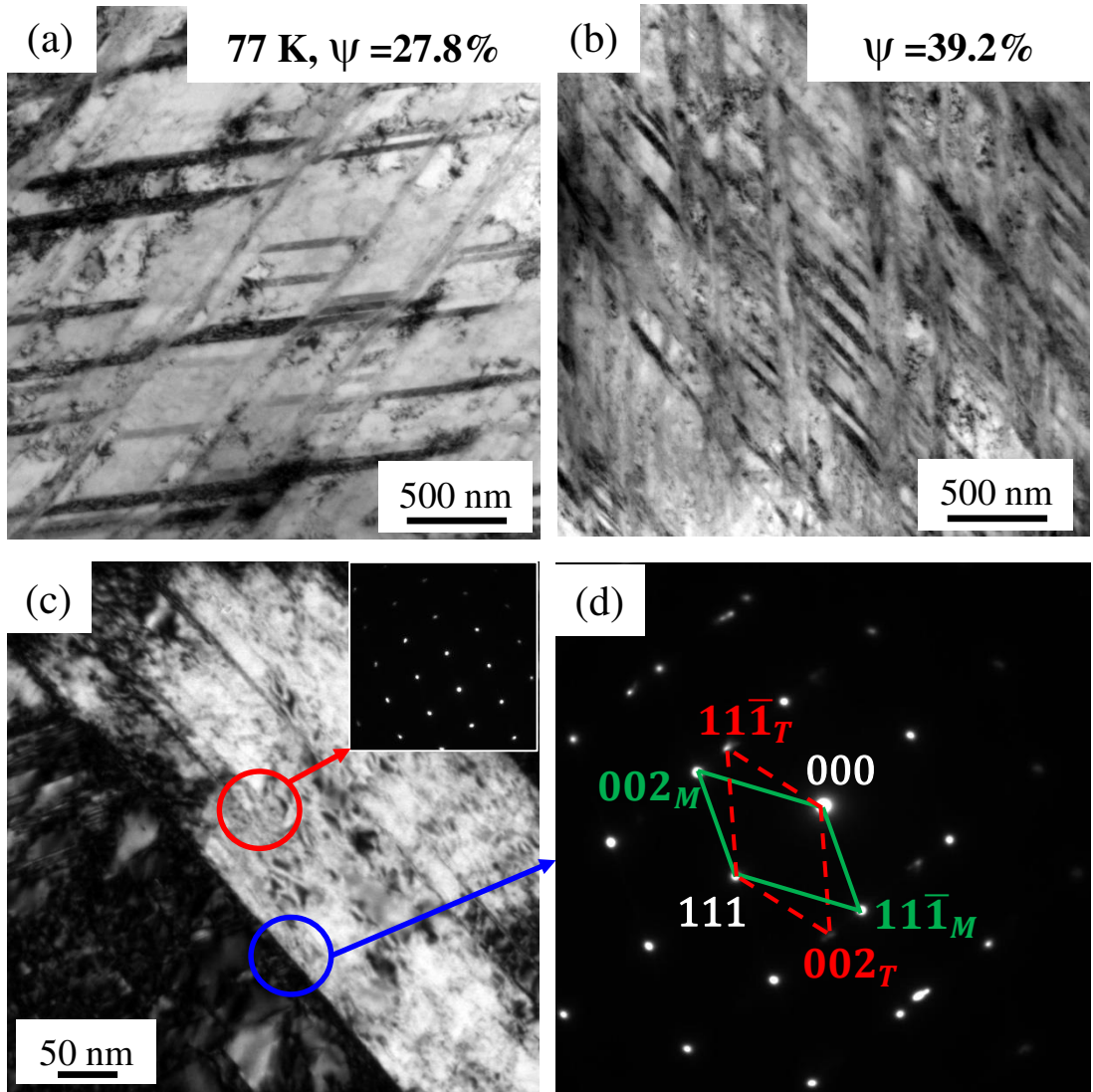


Fig. 7. TEM bright field micrographs of samples with (a) 27.8 % and (b) 39.2% strain at 77 K, which show nano-twins. (c) Higher magnification BF images with an inserted SAD pattern obtained from the matrix and (f) the composite SAD pattern obtained from the blue circled region in Fig. 7c which has contribution from both the matrix and the nano-twin.

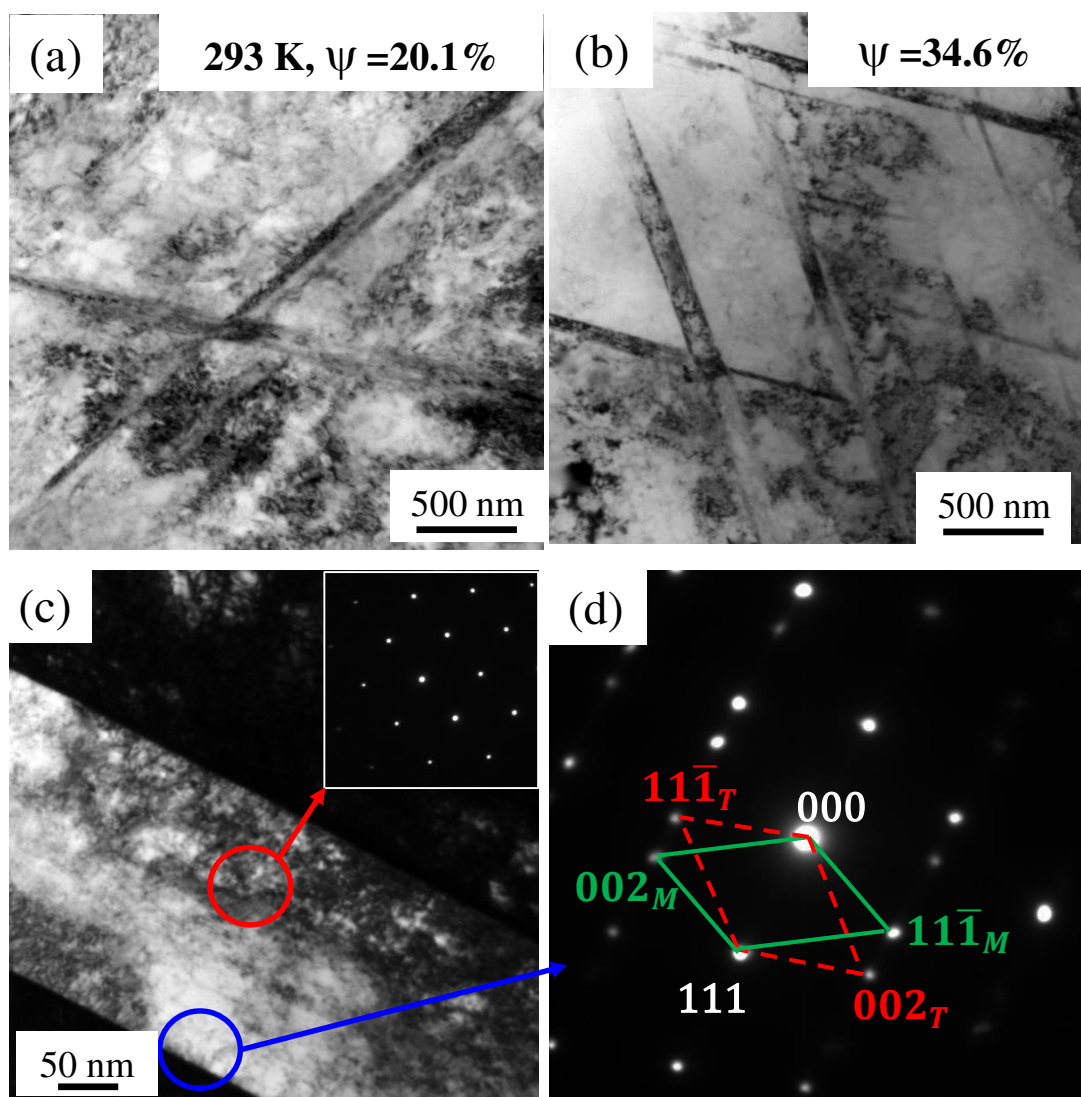


Fig. 8. TEM bright field micrographs of samples with (a) 20.1% and (b) 34.6% strain at 293k, which show nano-twins. (c) Higher magnification BF images with an inserted SAD pattern obtained from the matrix and (f) the composite SAD pattern obtained from the blue circled region in Fig. 8c which has contribution from both the matrix and the nano-twin.